Bulletin of the Seismological Society of America, Vol. XX, No. XX, pp. –, – 2018, doi: 10.1785/0120170342

Ⓔ

Stochastic Strong-Motion Simulation in Borehole and on Surface for the 2011 M_w 9.0 Tohoku-Oki Megathrust Earthquake Considering *P*, *SV*, and *SH* Amplification Transfer Functions

by Sergio Ruiz, Javier Ojeda, César Pastén, Cristian Otarola, and Rodrigo Silva

Abstract The 2011 Tohoku-Oki megathrust earthquake and its aftershocks were well recorded by the KiK-net network in accelerographs placed inside boreholes and on the surface. These data allow comparing strong-motion records with synthetic acceleration time histories for this large magnitude earthquake that caused extensive damage in Japan. Generating synthetic accelerograms at high frequencies can be approached using different techniques. We use the stochastic method to simulate horizontal and vertical strong-motion accelerograms in hard-rock boreholes; additionally, we incorporate *P*, *SV*, and *SH* soil amplification transfer functions to generate surface accelerograms. We reproduce the three components of the strong motion for 18 stations of the M_w 9.0 mainshock event; additionally, we simulated 8 stations for an M_w 6.9 aftershock. Our simulated acceleration time histories show similarity in time and frequency with the acceleration records for the period band between 0.05 and 1 s.

Electronic Supplement: Table of the velocity model used in the modeling of our synthetic records, and figures showing comparison of time series and 5% response spectra of synthetic and real data of 2011 Tohoku-Oki megathrust earthquake and an M_w 6.9 aftershock.

Introduction

K-NET and KiK-net networks recorded extensively the 2011 M_w 9.0 Tohoku-Oki megathrust earthquake and its aftershocks. The KiK-net stations, composed of surface and borehole accelerographs, allowed studying the behavior of soils during large earthquakes (Bonilla *et al.*, 2011; Ghofrani, Atkinson, and Goda, 2013; Roten *et al.*, 2013; Pavlenko, 2016). Proper modeling of the strong-motion records obtained in the borehole and on the ground surface is a challenge that can be approached using different strong-motion simulation techniques (Douglas and Aochi, 2008). One of the most accepted ground-motion simulation techniques is the stochastic approach, proposed by Boore (1983) and later improved in several studies (Beresnev and Atkinson, 1997; Boore, 2003; Motazedian and Atkinson, 2005; Otarola and Ruiz, 2016; among others). This method is based on the idea that the higher frequencies of ground motions have a random behavior that can be modeled in time and in frequency. The Brune (1970) source spectral model is used to modulate the hard-rock surface records in the frequency domain, whereas the soil influence is considered either intrinsically by the kappa or f_{max} parameters (Hanks, 1982; Anderson and Hough, 1984) or explicitly by adopting a spectral filter (Beresnev and Atkinson, 1998; Atkinson and Silva, 2000; Ghofrani, Atkinson, Goda, *et al.*, 2013; Otarola and Ruiz, 2016; and many others). The Tohoku-Oki earthquake showed a different emission of seismic waves pattern along-dip (Tajima *et al.*, 2013; Lay, 2017; and references therein). Apparently, the down-dip zone controlled the wavefield of strong-motion records. Kurahashi and Irikura (2011, 2013) and Asano and Iwata (2012) proposed that the strong motion was controlled by four or five strong-motion generation areas (SMGAs) of higher stress drop. Ghofrani, Atkinson, Goda, *et al.* (2013) used the proposed SMGAs and a random slip background or prescribed slip distribution to simulate the strong motion at borehole stations, using the EXSIM software (Motazedian and Atkinson, 2005; Boore, 2009) as well as amplification factors to obtain surface records (Ghofrani, Atkinson, and Goda, 2013). Here, we simulate 18 strong-motion records located in hard-rock boreholes and on the surface for the mainshock event and other 8 records for the M_w 6.9 aftershock that occurred on 23 June 2011 (Fig. 1). We follow the approach of Otarola and Ruiz (2016), who proposed considering *P* and *SV* waves, in addition to the *SH* waves, to improve the simulation of the three components, EW, NS, and UD, of borehole accelerograms. Additionally, we implemented the soil amplification transfer functions for *P*, *SV*, and *SH* waves proposed by Kausel

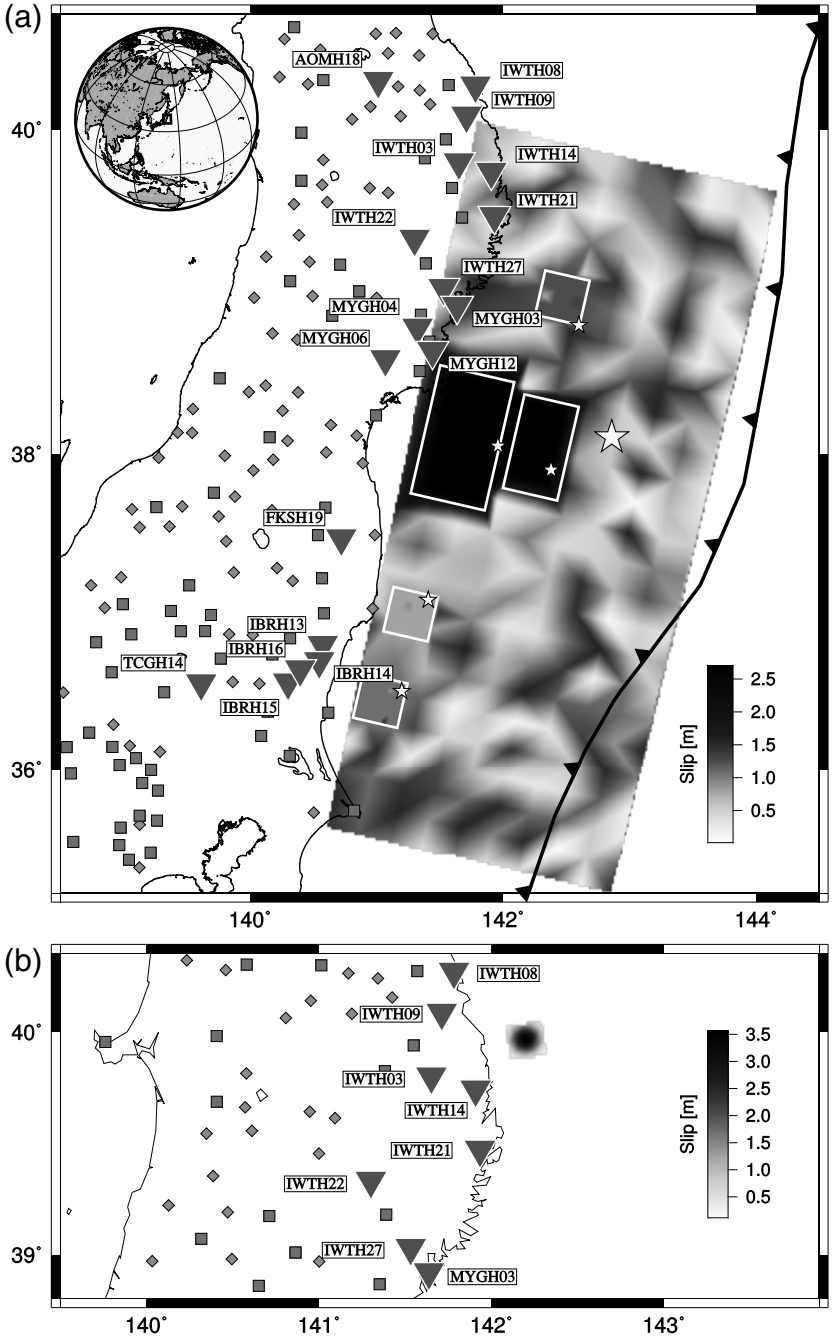

Figure 1. Slip distribution and KiK-net stations used for the simulations. Inverted triangles and square stations have $V_S > 1500$ m/s, and diamonds have $V_S < 1500$ m/s in the layer where the borehole sensor is placed is indicated. Larger inverted triangles are stations simulated in this work. (a) The finite-fault slip model of the 2011 M_w 9.0 Tohoku-Oki megathrust earthquake based on Ghofrani, Atkinson, Goda, *et al.* (2013), who used a random background slip in addition to the strong-motion generation area (SMGA) proposed by Kurahashi and Irikura (2011). The largest star indicates the epicenter, and the smaller stars are the epicenters of the SMGAs defined by Kurahashi and Irikura (2011; see Table 1). (b) The slip distribution of the Tohoku-Oki aftershock is represented by a 20 km × 20 km area. The hypocenter is in the center of the radial rupture (see Table 2).

and Roësset (1981) and Kausel (1994, 2006) to obtain the three components of strong-motion records on the ground surface.

Strong-Motion Data and Slip Distribution

We considered the KiK-net network stations because of their strong-motion data in boreholes, as well as the 1D-layered *S*-wave velocity (V_S) profiles. We used this information to compute the soil amplification transfer functions. We selected sites with V_S larger than 1500 m/s in the layer where the borehole sensor is placed. This strict criterion reduces the number of available stations, because the last layer is usually not hard rock ($V_S > 1500$ m/s). These V_S values ($V_S > 1500$ m/s) were chosen because our stochastic simulation method was originally defined for hard-rock sites, without soil amplification (Otarola and Ruiz, 2016). We discarded far-away stations from the coast and dominated by surface waves because our approach reproduces the body waves better than the surface waves (Otarola and Ruiz, 2016). A subgroup of stations with good azimuthal distribution and close to the fault is chosen for the simulations. Figure 1 shows all the KiK-net stations that satisfied our V_S criterion, as well as the 18 stations for the mainshock and the 8 stations for the aftershocks selected to the simulation. Figure 1a shows the SMGAs used for the M_w 9.0 Tohoku-Oki earthquake that were obtained from Kurahashi and Irikura (2011). A random slip distribution is added in the rectangle shown in Figure 1; the total slip distribution is consistent with a seismic moment of $M_0 = 4.02 \times 10^{22}$ N · m, equivalent to moment magnitude M_w 9.0 (Table 1). Figure 1b shows the slip distribution considered to simulate the 23 June 2011 aftershock. We applied a Gaussian slip model with a maximum displacement of 3.3 m and a radius of 10 km that correspond to a seismic moment of $M_0 = 2.85 \times 10^{19}$ N · m, equivalent to moment magnitude M_w 6.9, and we tested a stress drop of 3, 7, and 15 MPa (Table 2). The synthetic and recorded data are filtered between 0.01 and 20 Hz using a band-pass fourth-order Butterworth filter.

Table 1
Source Parameters of M_w 9.0 Tohoku-Oki Earthquake

Parameter	Value or Function	References
Hypocenter (latitude [°], longitude [°], and depth [km])	38.103, 142.860, and 23.7	JMA
Background plane (L [km], W [km], strike [°], dip [°], rake [°], and number of subfaults)	525, 235, 13, 10, 90, and 25 × 10	This study
Background slip distribution	Random slip	This study
SMGAs (L [km], W [km], strike [°], dip [°], depth [km], and subfaults [km × km])	62.4, 41.6, 13, 10, 28.03, and 6 × 4	Kurahashi and Irikura (2011)
	41.6, 41.6, 13, 10, 28.53, and 4 × 4	
	93.6, 52.0, 13, 10, 35.43, and 9 × 5	
	38.5, 38.5, 13, 10, 39.53, and 5 × 5	
	33.6, 33.6, 13, 10, 40.73, and 7 × 7	
Moment magnitude (M_w) for background and SMGAs	8.925, 8.21, 7.87, 8.39, 7.69, and 7.70	Kurahashi and Irikura (2011)
Stress drop (MPa) for background and SMGAs	3.5, 41.3, 23.6, 29.5, 16.4, and 26.0	Kurahashi and Irikura (2011) and Ghofrani, Atkinson, Goda, *et al.* (2013)
Rupture delay time for SMGAs (s)	15.64, 66.42, 68.41, 109.71, and 118.17	Kurahashi and Irikura (2011)
V_P and V_S velocity waves at the source depth (km/s)	6.95 and 3.95	Matsubara *et al.* (2008)
Rupture velocity (km/s)	2.88	Yagi and Fukahata (2011)
Density (g cm^{-3})	2.8	Ghofrani, Atkinson, Goda, *et al.* (2013)
Average of the radiation pattern for background slip	$< R^P >= 0.516$	Values deduced from the Onishi and Horike (2004) equations
	$< R^{SV} >= 0.535$	
	$< R^{SH} >= 0.325$	
Pulsing in percentage	100%	This study

JMA, Japan Meteorological Agency; SMGA, strong-motion generation area.

Table 2
Source Parameters of M_w 6.9 Tohoku-Oki Aftershock of 23 June 2011

Parameter	Value or Function	References
Hypocenter (latitude [°], longitude [°], and depth [km])	39.955, 142.205, and 33	NEIC
Background plane (L [km], W [km], strike [°], dip [°], rake [°], and number of subfaults)	20, 20, 189, 20, 90, 33, and 10 × 10	This study, NEIC for focal mechanism
Slip distribution	Gaussian distribution with maximum 3.4 m	This study
Moment magnitude (M_w)	6.9	JMA
Stress drop (MPa)	7.0 (3.0 and 15.0)	Seno (2014)
V_P and V_S velocity waves at the source depth	7.15 and 4.2	Matsubara *et al.* (2008)
Rupture velocity (km/s)	2.5	This study
Density (g cm^{-3})	3.2	This study
Average of the radiation pattern for background slip	$< R^P >= 0.516$	Values deduced from the Onishi and Horike (2004) equations
	$< R^{SV} >= 0.492$	
	$< R^{SH} >= 0.397$	
Pulsing in percentage	100%	This study

NEIC, National Earthquake Information Center.

Methodology

Our proposed methodology has two main steps. First, we simulated the strong-motion records in the location of the borehole sensor. We use the methodology proposed by Otarola and Ruiz (2016) to stochastically simulate *P*, *SV*, and *SH* waves. This stochastic simulation includes: (1) incident and azimuthal angles obtained from rays of *P* and *S* waves traced from the finite-fault discretized slip model to the station, passing through the regional layered stratified velocity model (see Ⓔ Table S1, available in the electronic supplement to this article), (2) free surface (FS) factors, and (3) energy partition (EP). We propagated the rupture considering for the mainshock a constant rupture velocity of 2.88 km/s (Table 2; Yagi and Fukahata, 2011) and the rupture delays of the SMGA proposed by Kurahashi and Irikura (2011). For the aftershock, a rupture velocity of 2.5 km/s was assumed (Table 2). Second, the stochastic *P*, *SV*, and *SH* waves generated on hard rock were convolved with the soil amplification transfer functions (SATFs) associated with

Table 3
Site Parameters of the Stations

Parameter	Value or Function	References
Kappa parameter	0.03 s	Ghofrani, Atkinson, Goda, *et al.* (2013)
Soil amplification	Transfer functions	Kausel and Roësset (1981) and Kausel (1994, 2006)

each type of waves. The SATF of *P*, *SV*, and *SH* waves were calculated between the surface and the depth where the borehole sensors were installed. The mathematical expressions were adapted from the works of Kausel and Roësset (1981) and Kausel (1994, 2006; Table 3). We used the shallow V_S velocity models of the KiK-net network for each station and inferred the V_P velocity model considering a constant Poisson ratio of 0.25. We fixed the soil damping to 10%. Here we describe in detail some parameters introduced in the proposed stochastic strong-motion simulation of Otarola and Ruiz (2016), adapted in this work.

Gaussian White Noise

Hanks and McGuire (1981) proposed that the high frequency of strong motion could be considered stochastic. We generated for each subfault of the fault plane a time-series-windowed white noise for *P*, *SV*, and *SH* waves. This time-series white noise is modulated using the acceleration envelope given by Saragoni and Hart (1974) (equation 1; Boore, 2003)

$$w(t;\epsilon,\eta,t_\eta) = a(t/t_\eta)^b \exp(-c(t/t_\eta)), \tag{1}$$

in which a, b, and c are: $a = (\frac{\exp(1)}{\epsilon})^b$, $b = -\frac{\epsilon \ln(\eta)}{[1+\epsilon(\ln(\epsilon)-1)]}$, $c = \frac{b}{\epsilon}$, $\epsilon = 0.25$, $\eta = 0.2$, $t_\eta = f_{T_{\rm gm}} \times T_{\rm gm}$, and $f_{T_{\rm gm}} = 0.3.T_{\rm gm}$ is the duration of the ground motion for *SH* waves as a function of the magnitude proposed by Ghofrani, Atkinson, Goda, *et al.* (2013) and Joshi (2014) (see Table 4). Because of lack of information for *P* waves, we consider the same approach for all types of waves.

P, *SV*, and *SH* Waves

Following the Aki and Richards (2002) notation, equations (2–4) show the generic far-field displacement for the *P*, *SV*, and *SH* waves propagating in the ray direction inside homogeneous elastic medium

$$u^P(x,t) = \frac{\mathcal{F}^P \dot{M}(t - R_{\rm hyp}/V_P)}{4\pi\rho\alpha^3 R_{\rm hyp}} \hat{I} \tag{2}$$

$$u^{SV}(x,t) = \frac{\mathcal{F}^{SV} \dot{M}(t - R_{\rm hyp}/V_S)}{4\pi\rho\beta^3 R_{\rm hyp}} \hat{p} \tag{3}$$

$$u^{SH}(x,t) = \frac{\mathcal{F}^{SH} \dot{M}(t - R_{\rm hyp}/V_S)}{4\pi\rho\beta^3 R_{\rm hyp}} \hat{\varphi}, \tag{4}$$

in which $\hat{I}$, $\hat{p}$, and $\hat{\varphi}$ are vector units in the directions of *P*, *SV*, and *SH* waves, respectively. $\hat{I}$ and $\hat{p}$ always are in the incident or vertical plane, and $\hat{\varphi}$ always is orthogonal to this plane. $\mathcal{F}^P$, $\mathcal{F}^{SV}$, $\mathcal{F}^{SH}$ are radiation patterns; $\dot{M}$ is the source time function; $R_{\rm hyp}$ is the hypocentral distance from the source to the observation point; ρ is the density in the source; α and β are *P*- and *S*-wave velocities in the source; and V_P and V_S are the average of the *P*- and *S*-wave velocities from source to the position x.

Shape-Noise Spectra Modeled by the $\omega^{-\gamma}$ Spectrum Model

In this next step, we consider the waves arriving at the surface; the FS and EP factors and trajectory and soil amplification parameters are included. Equations (2–4) are rotated in a new coordinated system composed of radial, tangential, and vertical directions (r, t, z). Then, we compute the Fourier transform of each time-series-windowed white noise record of each subfault normalized by the square root of the mean square amplitude spectrum. The spectra content is modulated by the same form that Boore (2003) proposed for *SH* waves.

Table 4
Path Parameters

Parameter	Value or Function	References
Duration for each seed ($T_{\rm gm}$)	$107.67 + 0.1208R_{\rm hyp}$ if $M_{\rm w} > 8.9$ $0.0015 \times 10^{0.5M_{\rm w}} + 0.02R_{\rm hyp}^{1.04}$ if $6.8 \le M_{\rm w} \le 7.4$	Ghofrani, Atkinson, Goda, *et al.* (2013) and Joshi (2014)
Geometric spreading $G(R_{ijm})$	$\frac{1}{R_{ijm}}$	Ghofrani, Atkinson, Goda, *et al.* (2013)
Quality factor of *S* wave (Q_S). Quality factor of *P* wave (Q_P) is deduced from equation (13): Fore-arc	$Q(f) = 300$ for $f \le 0.64$ Hz $Q(f) = 150(\frac{f}{1.0})^{1.3}$ for $f \ge 3.66$ Hz	Ghofrani, Atkinson, Goda, *et al.* (2013)
Quality factor of *S* wave (Q_S). Quality factor of *P* wave (Q_P) is deduced from equation (13): Back-arc	$Q(f) = 100$ for $f \le 0.20$ Hz $Q(f) = 165(\frac{f}{1.0})^{0.65}$ for $f \ge 0.39$ Hz	Ghofrani, Atkinson, Goda, *et al.* (2013)

Brune's expressions for *P*, *SV*, and *SH* waves are shown in the following equations:

$$A^{P}_{r_{ijml}} = \frac{\langle R^{P}\rangle_{ijm}\mathrm{FS}^{P}_{r_{ijm}}\mathrm{EP}^{P}_{r_{ijm}}M_{0ij}}{4\pi\rho\alpha^{3}}\frac{(2\pi f)^{2}}{1+\left(\frac{f}{f^{P}_{cij}}\right)^{\gamma}}G(R_{ijm}) \times \exp\left(-\frac{\pi R_{ijm}}{Q_{P}(f)\alpha}\right)\exp(-\pi f\kappa_{m})\mathrm{amp}(f)_{ml} \quad (5)$$

$$A^{P}_{z_{ijml}} = \frac{\langle R^{P}\rangle_{ijm}\mathrm{FS}^{P}_{z_{ijm}}\mathrm{EP}^{P}_{z_{ijm}}M_{0ij}}{4\pi\rho\alpha^{3}}\frac{(2\pi f)^{2}}{1+\left(\frac{f}{f^{P}_{cij}}\right)^{\gamma}}G(R_{ijm}) \times \exp\left(-\frac{\pi R_{ijm}}{Q_{P}(f)\alpha}\right)\exp(-\pi f\kappa_{m})\mathrm{amp}(f)_{ml} \quad (6)$$

$$A^{SV}_{r_{ijml}} = \frac{\langle R^{SV}\rangle_{ijm}\mathrm{FS}^{SV}_{r_{ijm}}\mathrm{EP}^{SV}_{r_{ijm}}M_{0ij}}{4\pi\rho\beta^{3}}\frac{(2\pi f)^{2}}{1+\left(\frac{f}{f^{S}_{cij}}\right)^{\gamma}}G(R_{ijm}) \times \exp\left(-\frac{\pi R_{ijm}}{Q_{S}(f)\beta}\right)\exp(-\pi f\kappa_{m})\mathrm{amp}(f)_{ml} \quad (7)$$

$$A^{SV}_{z_{ijml}} = \frac{\langle R^{SV}\rangle_{ijm}\mathrm{FS}^{SV}_{z_{ijm}}\mathrm{EP}^{SV}_{z_{ijm}}M_{0ij}}{4\pi\rho\beta^{3}}\frac{(2\pi f)^{2}}{1+\left(\frac{f}{f^{S}_{cij}}\right)^{\gamma}}G(R_{ijm}) \times \exp\left(-\frac{\pi R_{ijm}}{Q_{S}(f)\beta}\right)\exp(-\pi f\kappa_{m})\mathrm{amp}(f)_{ml} \quad (8)$$

$$A^{SH}_{t_{ijml}} = \frac{\langle R^{SH}\rangle_{ijm}\mathrm{FS}^{SH}_{t_{ijm}}\mathrm{EP}^{SH}_{t_{ijm}}M_{0ij}}{4\pi\rho\beta^{3}}\frac{(2\pi f)^{2}}{1+\left(\frac{f}{f^{S}_{cij}}\right)^{\gamma}}G(R_{ijm}) \times \exp\left(-\frac{\pi R_{ijm}}{Q_{S}(f)\beta}\right)\exp(-\pi f\kappa_{m})\mathrm{amp}(f)_{ml}, \quad (9)$$

in which A is the Brune spectra for the r, z, and t components of the *P*, *SV*, and *SH* waves. Superscript *P*, *SV*, and *SH* denotes *P*, *SV*, and *SH* waves. Subfaults are indicated by subscript ij. Stations are indicated by the subscript m, and the subscript l indicates whether the sensor position is in the borehole (B) or on the surface (S). R^{P}_{ijm}, R^{SV}_{ijm}, and R^{SH}_{ijm} are radiation coefficients. $\mathrm{FS}^{P}_{r_{ijm}}$, $\mathrm{FS}^{P}_{z_{ijm}}$, $\mathrm{FS}^{SV}_{r_{ijm}}$, $\mathrm{FS}^{SV}_{z_{ijm}}$, and $\mathrm{FS}^{SH}_{t_{ijm}}$ are FS factors, and $\mathrm{EP}^{P}_{r_{ijm}}$, $\mathrm{EP}^{P}_{z_{ijm}}$, $\mathrm{EP}^{SV}_{r_{ijm}}$, $\mathrm{EP}^{SV}_{z_{ijm}}$, and $EP^{SH}_{t_{ijm}}$ are the EP factors. M_{0ij} is the ijth subfault seismic moment. $G(R_{ijm})$ is the geometrical spreading (details in Table 4). $Q_S(f)$ and $Q_P(f)$ are the quality factors (details in Table 4). f^{S}_{cij} and f^{P}_{cij} are the dynamic corner frequencies. κ_m is the kappa factor (Table 3). $\mathrm{amp}(f)_{ml}$ is the soil amplification. If the station is in the borehole, $\mathrm{amp}(f)_{mB} = 1$, but if the station is on the surface, $\mathrm{amp}(f)_{mS} = \mathrm{SATF}_{mS}$, which is the soil amplification transfer function (see Table 3).

P-Wave Corner Frequency

Corner frequency of *P*-wave spectra is obtained from the relationship proposed by Hanks and Wyss (1972)

$$f^{P}_{c} = \frac{\alpha}{\beta}f^{S}_{c}, \quad (10)$$

in which f^{P}_{c} and f^{S}_{c} are corner frequencies for *P*- and *S*-wave spectra and α and β are *P*- and *S*-wave velocities at the source.

The same approach is used to obtain the dynamic corner frequency of *P* waves. The *S*-wave dynamic corner frequency was proposed by Motazedian and Atkinson (2005), as shown in equation (11). Using equations (10) and (11), we obtain equation (12) for the *P*-waves dynamic corner frequency

$$f^{S}_{cij} = 4.9\times10^{6}\beta\left[\frac{\Delta\sigma}{\min(\frac{N_R}{N}, F_{\mathrm{pulse}})\times M_0}\right]^{\frac{1}{3}} \quad (11)$$

$$f^{P}_{cij} = \frac{\alpha}{\beta}f^{S}_{cij}, \quad (12)$$

in which f^{P}_{cij} and f^{S}_{cij} are corner frequencies for *P*- and *S*-wave spectra of the ij subfault, M_0 is the seismic moment, $\Delta\sigma$ is the stress drop, N is the number of the subfault, N_R is the accumulative number of subfaults active in time t, and F_{pulse} is the maximum percentage of active subfaults during the rupture (Tables 1 and 2).

P-Waves Quality Factor

We consider the relationship proposed by Udias (1999) to obtain a *P*-wave quality factor Q_P from the *S*-wave quality factor Q_S

$$\frac{1}{Q_P} = \frac{4}{3}\frac{\beta^{2}}{\alpha^{2}}\frac{1}{Q_S}, \quad (13)$$

in which α and β are *S*- and *P*-wave velocities at the source depth (see details in Table 4).

Radiation Pattern

Explicit values of the radiation pattern for *P*, *SV*, and *SH* waves can be deduced in terms of the main angles of the fault plane (strike, dip, and rake) and emergence and azimuthal angles (Aki and Richards, 2002). In general, for stochastic methods, the values are derived as the average of the radiation coefficients (Boore and Boatwright, 1984). Here, we use the theoretical isotropic values for high-frequency *P*, *SV*, and *SH* waves (equations 14–16) proposed by Onishi and Horike (2004)

$$\langle R^{P}\rangle_{ijm} = \sqrt{\frac{4}{15}} \quad (14)$$

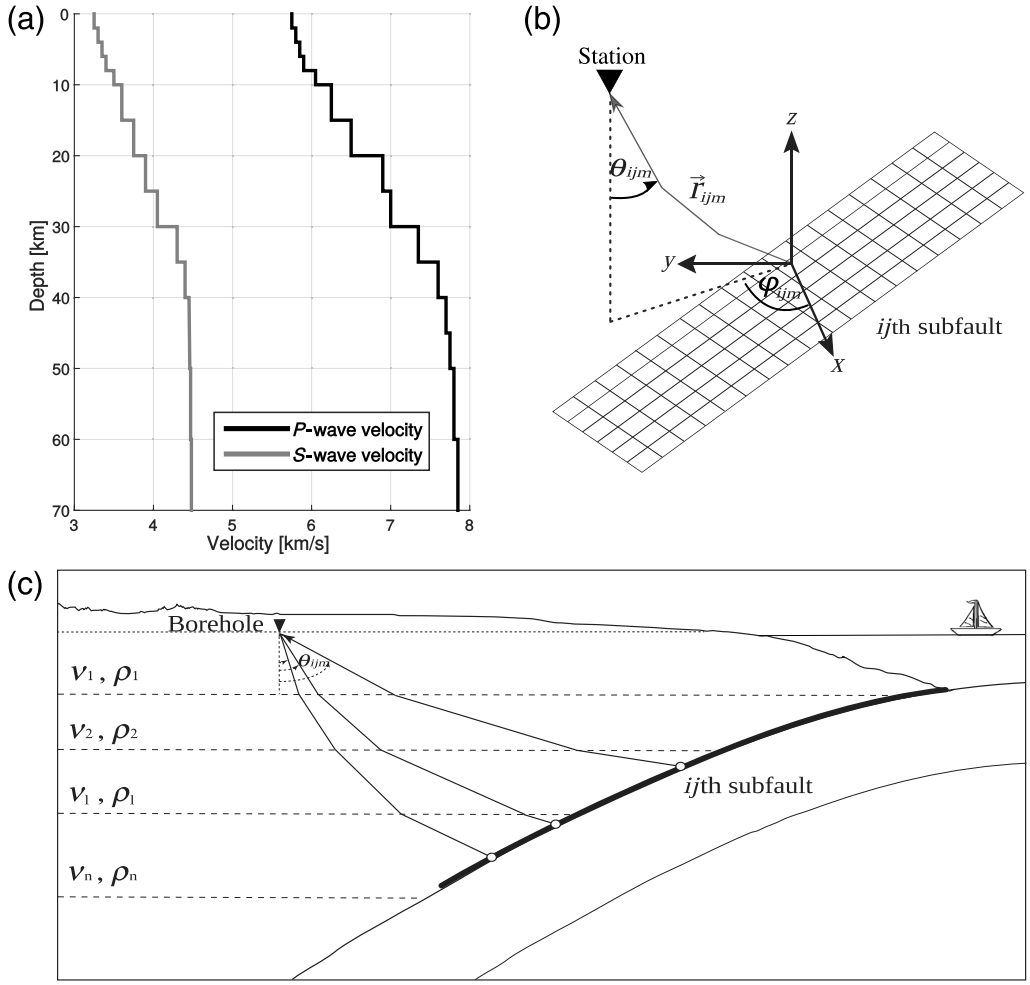

Figure 2. Schematic direct ray propagation through 1D regional velocity layer in a subduction profile of Japan. (a) *P*- and *S*-wave velocity model considered in this work (Ⓔ Table S1, available in the electronic supplement to this article). (b) Azimuthal φ_{ijm} and incident θ_{ijm} angles derived from a ray r_{ijm} traveling from subfault ij to station m. (c) Direct ray propagation in a profile of the subduction of Japan.

$$\langle R^{SV}\rangle_{ijm} = \frac{1}{2}\sqrt{\sin^2(\lambda)\left(\frac{14}{15}+\frac{1}{3}\sin^2(2\delta)\right)+\cos^2(\lambda)\left(\frac{4}{15}+\frac{2}{3}\cos^2(\delta)\right)} \tag{15}$$

$$\langle R^{SH}\rangle_{ijm} = \frac{1}{2}\sqrt{\frac{2}{3}\cos^2(\lambda)(1+\sin^2(\delta))+\frac{1}{3}\sin^2(\lambda)(1+\cos^2(2\delta))}, \tag{16}$$

in which (δ) is the dip angle and (λ) is the rake angle (see Tables 1 and 2). In this work, we use the same radiation pattern for all subfaults and stations position.

Incident and Azimuthal Angles

The stochastic strong-motion simulation method proposed originally by Boore (1983, 2003) considers only *SH* waves. In such a case, the incident angles can be considered as vertical incident angles, and the EP can be considered equal for both horizontal components. Our formulation adds the *P* waves and incident angles of direct seismic rays from the source to the station. This implies that the *S* wave must be decomposed into *SH* and *SV* waves and that the EP must be estimated as a function of the incident and azimuthal angles. To obtain these angles, we consider direct rays propagating from the centroid of each subfault through a 1D regional velocity model to the station. We built a matrix composed by incident and azimuthal angles for each subfault and for each station considered in our simulations. Figure 2 shows schematically a subduction profile of Japan. Along dip and strike, a ray from each subfault is traced to the station describing a trajectory following the Snell law.

Free Surface Factors

In our simulations, *P* and *S* waves arrive at a station with an incident angle not vertical. The FS factor of *SH* waves is always 2, and for radial and vertical *SV* and *P* waves, the values depend on the incident angles (Evans, 1984; Jiang

et al., 1998). For the Tohoku-Oki mainshock and the aftershock earthquakes, we derive a range of incident angles between 12° and 52° that include large values of surface factors for radial *SV* waves and values close to zero for radial and vertical *SV* waves (see Fig. 3).

Energy Partition

EP factors depend on the incident angle, the position of the subfault, and the location of the station. The EP for radial and vertical *P*-wave rays are shown in equations (17) and (18), whereas the EP for radial and vertical *SV*-wave rays are shown in equations (19) and (20). The EP of an SH tangential ray is equal to 1 (equation 21):

$$\mathrm{EP}^{P}_{r_{ijm}} = -\sin(\theta_{ijm}) \tag{17}$$

$$\mathrm{EP}^{P}_{z_{ijm}} = \cos(\theta_{ijm}) \tag{18}$$

$$\mathrm{EP}^{SV}_{r_{ijm}} = \cos(\theta_{ijm}) \tag{19}$$

$$\mathrm{EP}^{SV}_{z_{ijm}} = \sin(\theta_{ijm}) \tag{20}$$

$$\mathrm{EP}^{SH}_{t_{ijm}} = 1. \tag{21}$$

θ_{ijm} is the incident angle of *P* or *S* waves for the subfault ij at the station m.

Scaling Factors

Scaling factors are introduced to balance and conserve the total radiated energy from the subfaults at high frequencies. To obtain the *P*-waves scaling factor (H^P), we follow the *S*-waves scaling factor (H^S) proposed by Motazedian and Atkinson (2005); however, here, we have considered that the total radiated energy is given by the sum of the radiated energy of the *S* and *P* waves. H^P and H^S are shown in the following equations:

$$H^{P}_{ij} = \frac{M_0}{M_{0ij}} \sqrt{\frac{1}{N} \frac{\Sigma_{f_k}\left[\frac{f_k^2}{1+\left(\frac{f_k}{f^P_c}\right)^{\gamma}}\right]^2}{\Sigma_{f_k}\left[\frac{f_k^2}{1+\left(\frac{f_k}{f^P_{cij}}\right)^{\gamma}}\right]^2}} \tag{22}$$

$$H^{S}_{ij} = \frac{M_0}{M_{0ij}} \sqrt{\frac{1}{N} \frac{\Sigma_{f_k}\left[\frac{f_k^2}{1+\left(\frac{f_k}{f^S_c}\right)^{\gamma}}\right]^2}{\Sigma_{f_k}\left[\frac{f_k^2}{1+\left(\frac{f_k}{f^S_{cij}}\right)^{\gamma}}\right]^2}}, \tag{23}$$

in which f_k is the kth frequency, M_{0ij} is the ijth subfault seismic moment (if all subfaults are identical, then $M_{0ij} = M_0/N$), and γ is equal to 2, because we considered the Brune's model.

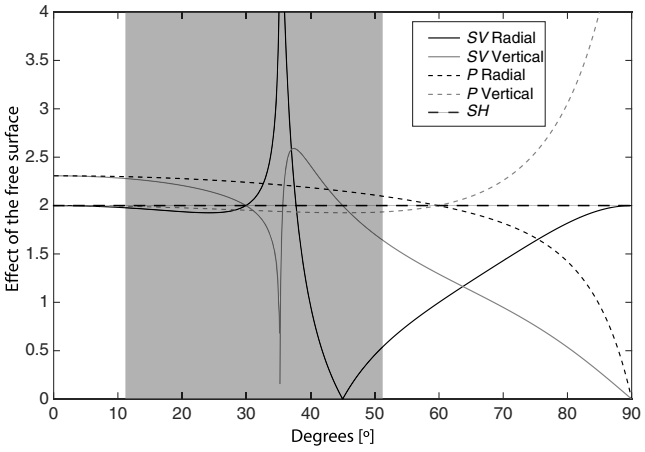

Figure 3. Free surface factors of *P*, *SV*, and *SH* waves as a function of incident angles. The gray zone is the range of incident angles that we compute in this work for the M_w 9.0 Tohoku-Oki mainshock and the 23 June 2011 M_w 6.9 earthquakes.

Acceleration Time Series

We applied the inverse Fourier transform of *P*, *SV*, and *SH* radial, tangential, and vertical waves associated with each station and each subfault ij (equations 5–9). Then, we summed the strong-motion time series associated with each subfaults, considering the H^P and H^S scaling factors, the phase associated with the time rupture (t_{Rij}) of the ijth subfault, and the travel time of the seismic waves (*P* and *S*) to the station m (t^P_{ijm} and t^S_{ijm}). The time phases are

$$\Delta t^{P}_{ijm} = t_{Rij} + t^{P}_{ijm} \tag{24}$$

$$\Delta t^{S}_{ijm} = t_{Rij} + t^{S}_{ijm}, \tag{25}$$

in which Δt^P_{ijm} and Δt^S_{ijm} are the relative time delay for the *P* and *S* waves from the ij subfault to the station m.

The *P*, *SV*, and *SH* strong-motion time series in the radial, tangential, and vertical coordinate system at each station m are indicated in the following equations:

$$a^{P}_{r_{ijm}} = a^{P}_{r_{ijm}}(t + \Delta t^{P}_{ijm}) \times H^{P}_{ij} \tag{26}$$

$$a^{P}_{z_{ijm}} = a^{P}_{z_{ijm}}(t + \Delta t^{P}_{ijm}) \times H^{P}_{ij} \tag{27}$$

$$a^{SV}_{r_{ijm}} = a^{SV}_{r_{ijm}}(t + \Delta t^{S}_{ijm}) \times H^{S}_{ij} \tag{28}$$

$$a^{SV}_{z_{ijm}} = a^{SV}_{z_{ijm}}(t + \Delta t^{S}_{ijm}) \times H^{S}_{ij} \tag{29}$$

$$a^{SH}_{t_{ijm}} = a^{SH}_{t_{ijm}}(t + \Delta t^{S}_{ijm}) \times H^{S}_{ij}. \tag{30}$$

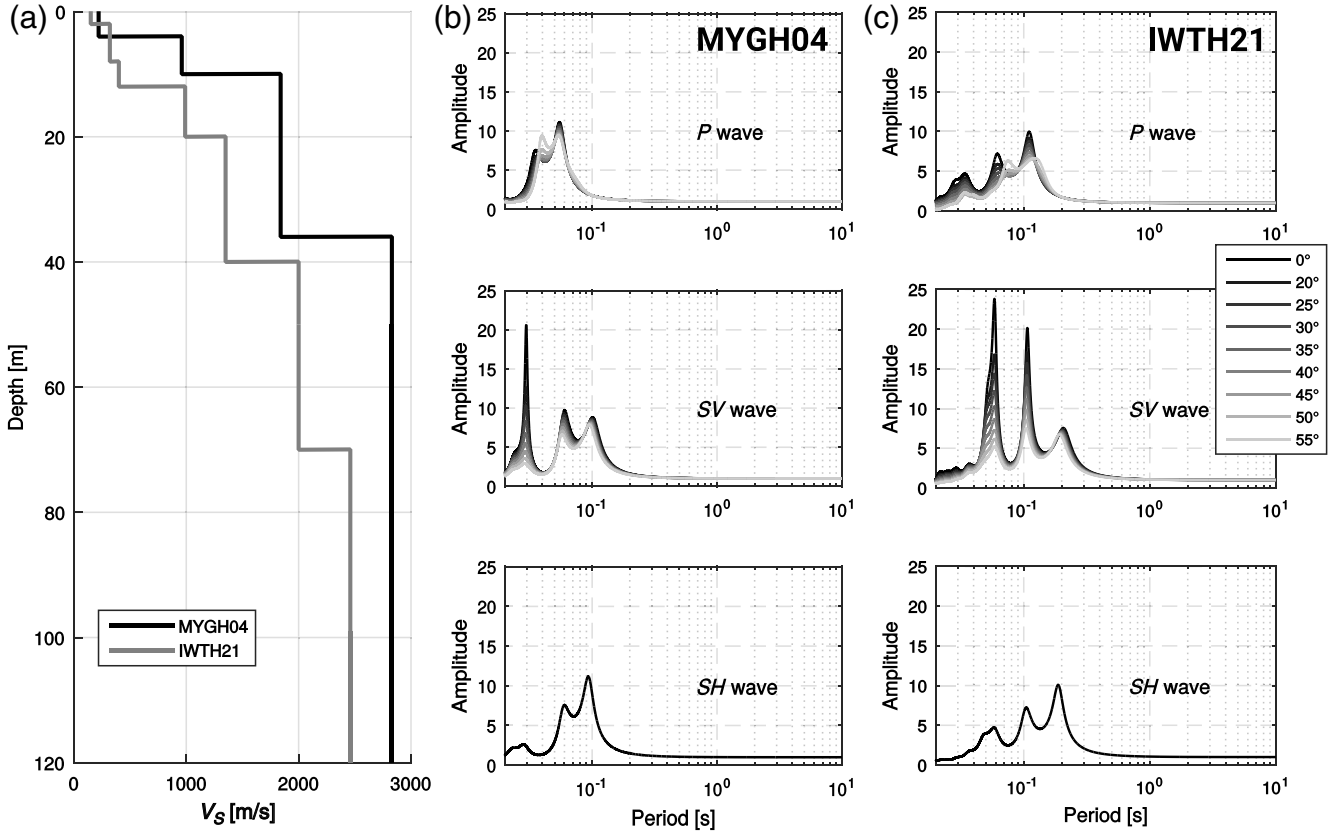

Figure 4. (a) *S*-wave velocity model of the MYGH04 and IWTH21 stations. The depth of the borehole instruments is at 100 m. (b,c) Soil amplification transfer functions for *P*, *SV*, and *SH* waves of each station. The soil amplification transfer functions are plotted for different incident angles.

Then, equations (26–30) are rotated in the east–west (EW), north–south (NS), and vertical (up–down [UD]) directions, considering the azimuthal angles of each ray arriving at the station m from each subfault ij. From equation (31), we can obtain equations (32–34)

$$\begin{pmatrix} a_{ijm}^{X-\mathrm{NS}} \\ a_{ijm}^{X-\mathrm{EW}} \\ a_{ijm}^{X-\mathrm{UD}} \end{pmatrix} = \begin{pmatrix} \cos(\phi_{ijm}) & -\sin(\phi_{ijm}) & 0 \\ \sin(\phi_{ijm}) & \cos(\phi_{ijm}) & 0 \\ 0 & 0 & 1 \end{pmatrix} \begin{pmatrix} a_{r_{ijm}}^{X} \\ a_{t_{ijm}}^{X} \\ a_{z_{ijm}}^{X} \end{pmatrix} \tag{31}$$

$$a_{ijm}^{X-\mathrm{NS}} = a_{r_{ijm}}^{X} \cos(\phi_{ijm}) - a_{t_{ijm}}^{X} \sin(\phi_{ijm}) \tag{32}$$

$$a_{ijm}^{X-\mathrm{EW}} = a_{r_{ijm}}^{X} \sin(\phi_{ijm}) + a_{t_{ijm}}^{X} \cos(\phi_{ijm}) \tag{33}$$

$$a_{ijm}^{X-\mathrm{UD}} = a_{z_{ijm}}^{X}, \tag{34}$$

in which the superscript X can be a *P*, *SV*, or *SH* wave.

Finally, we summed all waves associated with each subfault ij in the station m

$$a_m^{\mathrm{NS}} = \sum_{i=1}^{N_L} \sum_{j=1}^{N_W} a_{ijm}^{P-\mathrm{NS}} + a_{ijm}^{SV-\mathrm{NS}} + a_{ijm}^{SH-\mathrm{NS}} \tag{35}$$

$$a_m^{\mathrm{EW}} = \sum_{i=1}^{N_L} \sum_{j=1}^{N_W} a_{ijm}^{P-\mathrm{EW}} + a_{ijm}^{SV-\mathrm{EW}} + a_{ijm}^{SH-\mathrm{EW}} \tag{36}$$

$$a_m^{\mathrm{UD}} = \sum_{i=1}^{N_L} \sum_{j=1}^{N_W} a_{ijm}^{P-\mathrm{UD}} + a_{ijm}^{SV-\mathrm{UD}}. \tag{37}$$

Soil Amplification Transfer Function

The surface records are obtained from borehole strong-motion records, convolved with the SATF proposed by Kausel and Roësset (1981) and Kausel (1994, 2006). The SATF for each station depends on the local soil velocity profile. In addition, the amplitudes are also function of the incident angle for *P* and *SV* waves. In this work, we consider a soil damping of 10%, but more detailed geotechnical studies could improve this value. Figure 4 shows the velocity profiles and SATF of the MYGH04 and IWTH21 stations. The lower periods have a larger variability with the incident angles. These variations can be larger than five times, in the range of incident angles considered in this work for the Tohoku-Oki earthquakes. On the other hand, the soil amplification on the surface is several times larger than the bore-

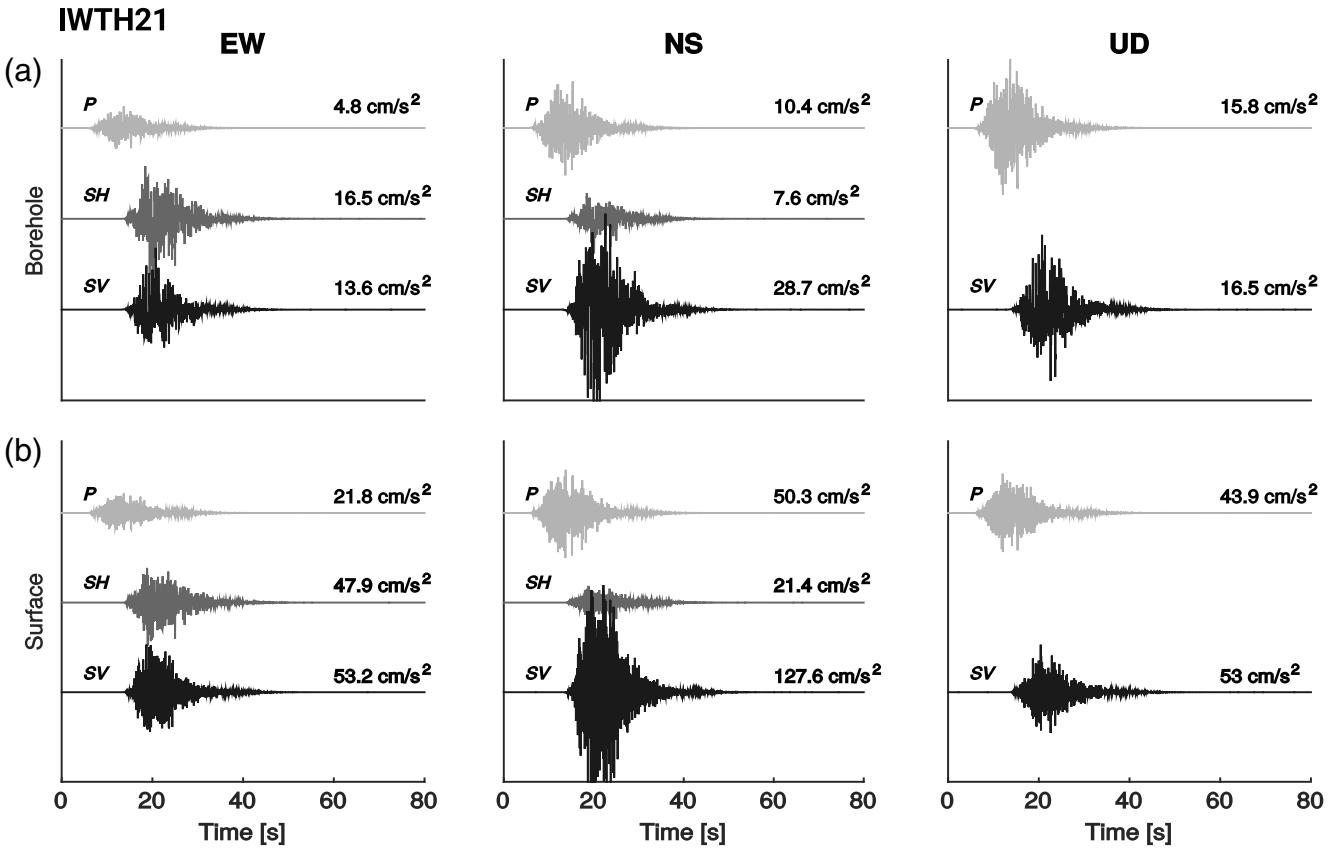

Figure 5. *P*, *SH*, and *SV* waves generated for the 23 June Tohoku-Oki aftershock in the IWTH21 station. The numbers are peak ground acceleration (PGA) values. (a) Borehole strong motion; (b) surface strong motion.

hole amplitudes for the fundamental soil period and in some case for the soil higher-vibration modes. The rest of stations considered in this work show similar values of amplification between borehole hard rock and the surface (see Ⓔ Fig. S1).

Results

We generated strong-motion records in the borehole and on the surface. The proposed methodology incorporated new parameters that allow simulating *P*, *SV*, and *SH* waves. First, we simulated the accelerograms of the M_w 6.9 aftershock of 23 June 2011. We modeled it as the rupture of only one asperity (Tables 2 and 4). We test three different stress-drop values (3, 7, and 15 MPa); we prefer considering 7 MPa because we obtain a better fit between synthetic and real data. The simulation using 3 MPa underestimates the accelerations, and, on the other hand, the stress drop of 15 MPa overestimates the results (see Ⓔ Fig. S4). Nonetheless, more detailed seismological studies are necessary, because our simulations depend strongly on the kinematic history of the slip distribution of every earthquake. Figure 5 shows the simulation of *P*, *SV*, and *SH* waves in boreholes and on the surface considering the EW, NS, and UD coordinate system on Station IWTH21. For the Tohoku-Oki megathrust earthquake, we considered the rupture and geometrical parameters proposed previously (Tables 1, 3, and 4). Figure 6 shows the results of our simulation on the MGYH04 station. In both figures, we can observe that the *P*, *SV*, and *SH* time-series phases and amplitudes for the three types of waves are not the same because of the differences between V_P and V_S velocities, EP, FS, etc.

The final synthetic records are shown in Figures 7 and 8 and in Ⓔ Figures S2 and S3. In the same figures, the recorded data for the 18 KiK-net selected stations for the mainshock and the 8 KiK-net selected stations for the aftershock (Fig. 1) are shown. Time-series shapes are comparable between observed and simulated records. For the aftershock and mainshock, the main characteristics are reproduced by the synthetic records reproducing the larger high-frequency energy burst associated with the SMGAs. The peak ground acceleration (PGA) differences between synthetic and recorded data are small in each component, with the exception of the FKSH19 station for the mainshock and the IWTH09 and the IWTH14 stations for the aftershock and the mainshock. In general, a slight trend of underestimation of the PGA for the synthetic records is observed (Fig. 9a). Figures 7 and 8 show some similarity between the observed and the simulated three-component accelerograms and acceleration response spectra (5% of the critical damping). The 5% acceleration response spectra of the borehole and the surface records have larger pseudospectral amplitudes in different periods, because of the soil amplifications introduced by the transfer functions. In several records, the synthetic spectral

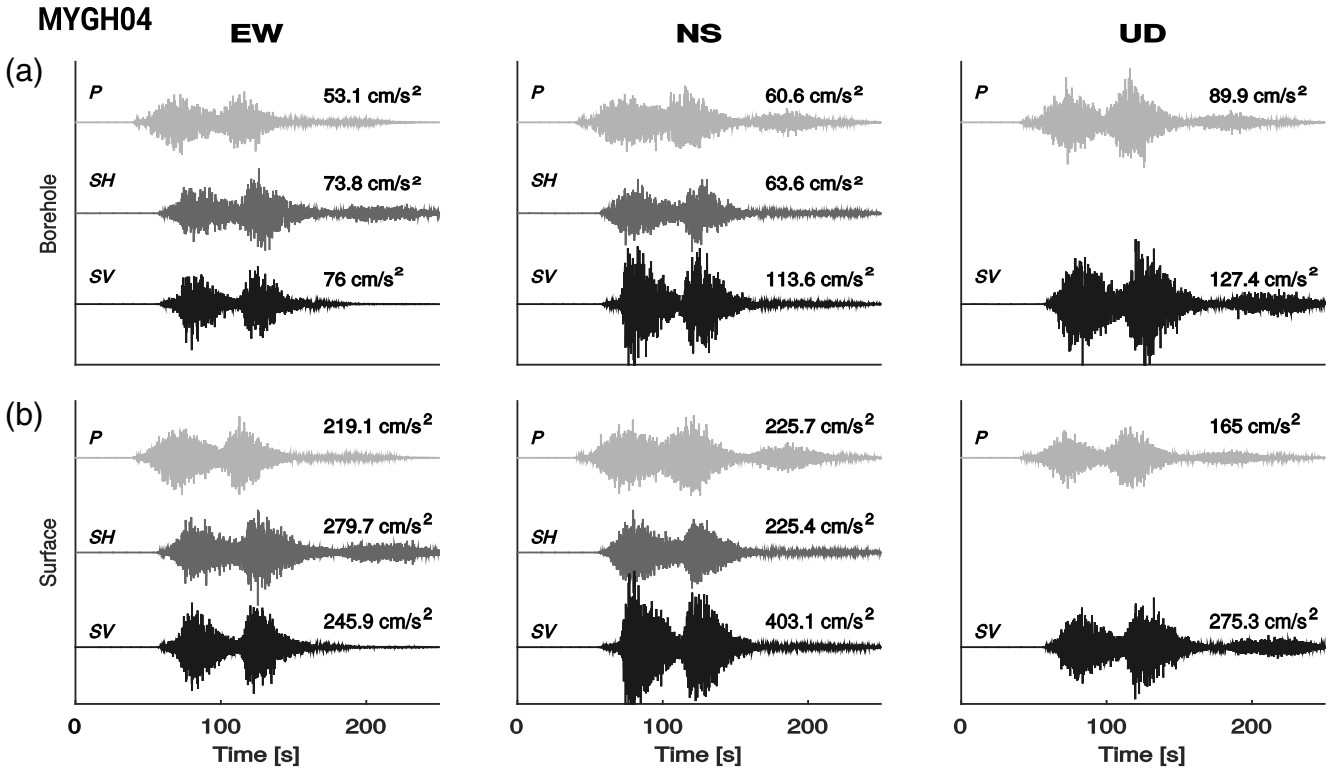

Figure 6. *P*, *SH*, and *SV* waves generated for the Tohoku-Oki mainshock in the MYGH04 station. The numbers are PGA values. (a) Borehole strong motion; (b) surface strong motion.

peaks do not coincide with those of the recorded data, despite the overall good fit. To validate the frequency fit in the stations, we calculated the goodness of fit (GOF; Graves and Pitarka, 2010) (equations 38 and 39)

$$B(T_k)^Y = \frac{1}{N}\sum_{m=1}^{N} \ln\left(\frac{O_m^Y(T_k)}{S_m^Y(T_k)}\right) \tag{38}$$

$$\sigma(T_k)^Y = \sqrt{\left(\frac{1}{N}\sum_{m=1}^{N}\left[\ln\left(\frac{O_m^Y(T_k)}{S_m^Y(T_k)}\right) - B(T_k)^Y\right]^2\right)}, \tag{39}$$

in which $B(T_k)^Y$ is GOF, O_m^Y is the observed record in the station m, and S_m^Y is the simulated record in the station m, $\sigma(T_k)^Y$ is the standard deviation, T_k is the period k, N is the number of stations, and Y can be the EW, NS, or UD component. We observe a good fit for the periods between 0.05 and 1 s for the borehole and the surface records and the large period spectral behavior (> 1 s) of our simulations overestimating the ground motion (see Fig. 9).

Discussion

For the surface synthetic strong-motion time series of the aftershock (Fig. 5), the amplitude of the *SV* waves is larger than *P* and *SH* waves because of the amplitude modification produced by the soil amplification transfer functions of the IWTH21 station shown in Figure 4. In other cases, we observe larger values of *P* waves in the horizontal components in comparison with the *P*-wave amplitude of the vertical component. These results are strongly controlled by the values of the incident angle and the radiation pattern. We propose in future works introducing more realistic 3D velocity models to better constrain the incident angles, and computing stochastic radiation patterns for the high frequencies in more detailed, for example, radiation patterns proposed by Pulido and Kubo (2004). Our simulations do not reproduce farther stations well, probably because we do not model surface waves. We propose introducing reflected and refracted rays in the next works.

Some parameters where fixed due to lack of specific studies. For example, we fixed kappa values and soil damping, using the same values in all the sites. We use the same duration function for the strong motion of each subfault derived for *S* waves by Ghofrani, Atkinson, Goda, *et al.* (2013) and Joshi (2014) to model the duration of *P* waves. These parameters can be improved.

We generate high-frequency strong-motion records for the 2011 Tohoku-Oki megathrust M_w 9.0 earthquake and the 23 June 2011 M_w 6.9 aftershock. Previously, Ghofrani, Atkinson, Goda, *et al.* (2013) successfully reproduced strong-motion records of the M_w 9.0 earthquake using the stochastic approach. The most prominent difference between our work and Ghofrani, Atkinson, Goda, *et al.* (2013) is that here we simulated strong-motion accelerograms in the three components (EW, NS, and UD) considering stochastic *P*, *SV*, and *SH* waves, instead of the stochastic *SH* waves only that

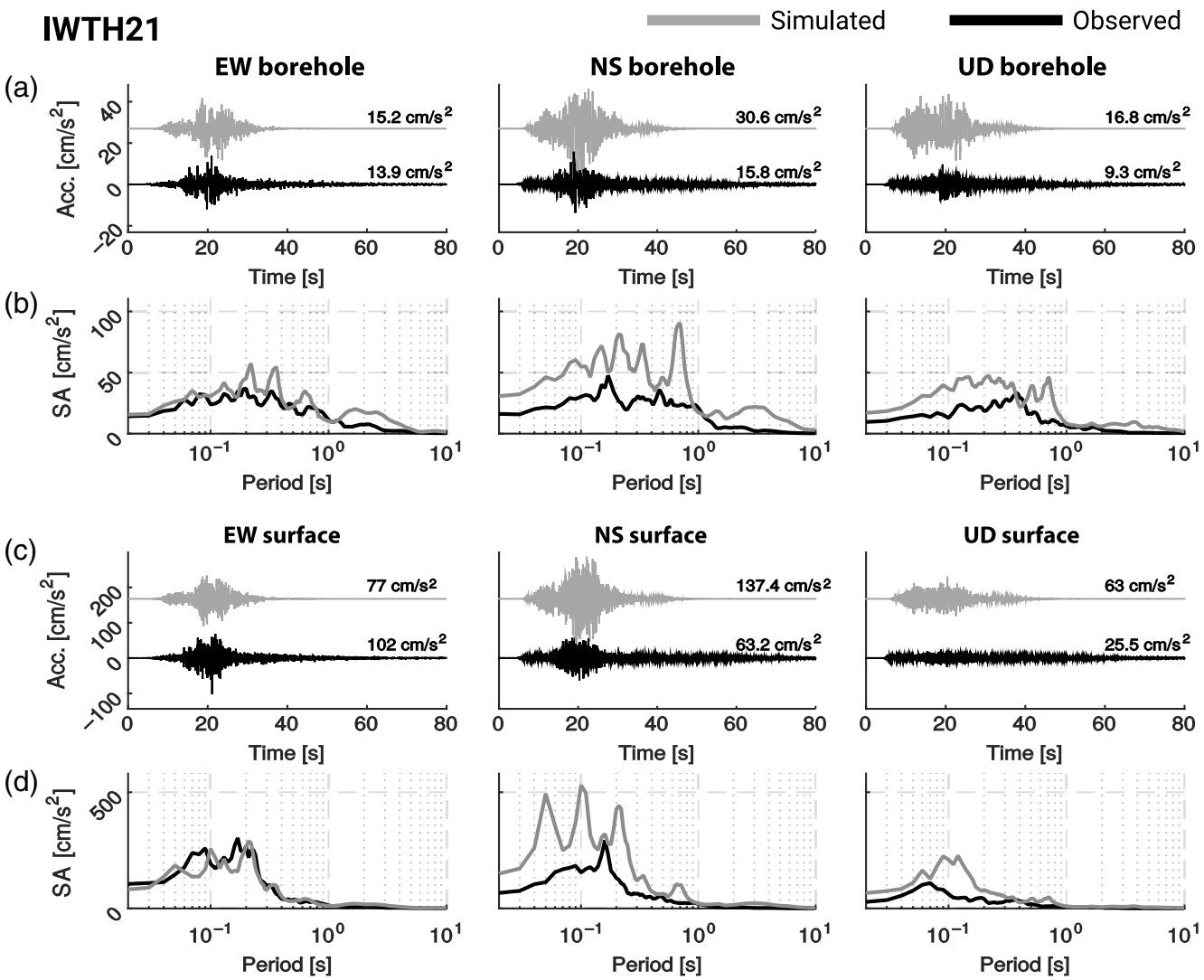

Figure 7. Comparison between observed and simulated three-component records on the surface and in the borehole of the IWTH21 station for the 23 June 2011 Tohoku-Oki aftershock. (a) Borehole accelerograms; (b) borehole 5% response spectra, (c) surface accelerograms; (d) surface 5% response spectra.

generate a generic horizontal component. On the other hand, the decomposition in *P*, *SV*, and *SH* waves allows us to generate surface records modulating the borehole hard-rock synthetic records using the soil amplification transfer functions proposed by Kausel (2006). The synthetic surface records (Figs. 7 and 8, and Ⓔ Figs. S2 and S3) have some spectral differences with respect to the real records for some particular periods. In some cases, we observe clear spectral peaks in the synthetic records that do not exist in the real records. This distortion is probably associated with incorrect velocity soil profile, 3D, or nonlinear effects. In particular, nonlinear effects have been detected in some records for the M_w 9.0 Tohoku-Oki earthquakes (Roten *et al.*, 2013; Pavlenko, 2016). On the other hand, we considered that our simulations in hard rock do not present any type of soil amplification, which is a very strong assumption that we should improve.

We observe that acceleration records data of the M_w 9.0 Tohoku-Oki have two pulses of larger amplitudes. This shape is well modeled by synthetic records, validating the finite fault used in this work, previously proposed by Ghofrani, Atkinson, Goda, *et al.* (2013). Then, for the 18 simulated stations, mostly high frequency of strong-motion records would come from the two larger slip SMGA located just underneath the hypocenter. For the M_w 6.9 aftershock, we consider an asperity with a Gaussian slip distribution. In addition, the parameters used in the inversion can be different, a cause of trade-off between the rupture area and the velocity rupture. We finally use a velocity rupture of 2.5 km/s and a rectangular rupture area of 20 km × 20 km, but other combinations are possible to generate synthetic records that fit well the recorded data. We tested three different stress-drop values that have a direct incidence in the acceleration amplitude of the simulated time series; because of that this parameter control the dynamic corner frequency associated with each subfault (equation 11). A realistic value of the stress drop is critical to adjust the amplitude of the simulated records, whereas a realistic slip

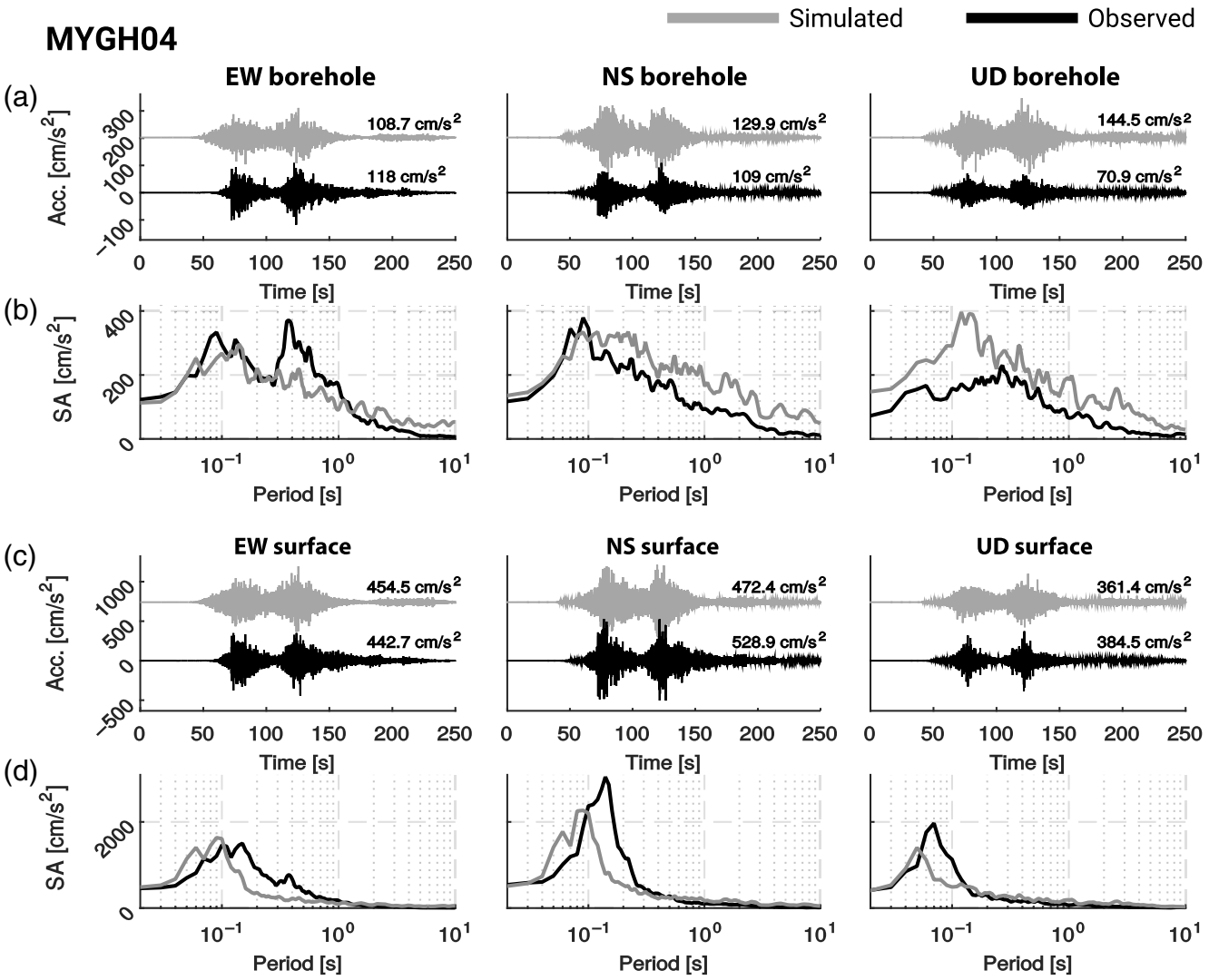

Figure 8. Comparison between observed and simulated three-component records on the surface and in the borehole of the MYGH04 station of the M_w 9.0 Tohoku-Oki mainshock. (a) Borehole accelerograms; (b) borehole 5% response spectra, (c) surface accelerograms; (d) surface 5% response spectra.

distribution history is critical to fit the time-history shape. The eight KiK-net stations simulated for the aftershock were also simulated for the mainshock. However, we do not observe a tendency in our simulations for a same station. This occurs because some parameters, such as incident angles, FS, and EP, are different for each event in the same site.

Long periods are overestimated by our methodology; this is clear in the GOF (see Fig. 9). This is a consequence that we do not consider a proper slip distribution model for long periods, which is beyond the scope of this work. We consider that the stochastic methodology is not useful for longer periods (> 1 s) that can be simulated using deterministic methods. Combining the long periods with the short-period stochastic approach has been proposed in hybrid simulations (e.g., Kamae *et al.*, 1998; Douglas and Aochi, 2008; and many others). Our proposed methodology can enhance the combination of both approaches. Here, the stochastic generation of the three components allows combining the deterministic and stochastic approaches directly simulating EW, NS, and UD strong-motion components. Finally, we believe that the *P*, *SV*, and *SH* soil amplification transfer functions are useful to model synthetic accelerograms in sites where only downhole seismic velocity profiles are available.

Conclusions

We introduce more physical parameters in the synthetic generation of strong-motion records than the classic stochastic strong-motion approach. The methodology presented herein is an improvement of the stochastic method originally proposed by Boore (1983) (Beresnev and Atkinson, 1997; Boore, 2003; Motazedian and Atkinson, 2005) and develops in detail the modifications introduced by Otarola and Ruiz (2016) to simulate stochastically *P* and *SV* waves. The simulation of *P*, *SV*, and *SH* stochastic waves allow us to incorporate SATF (Kausel, 2006) and simulate synthetic three-component surface

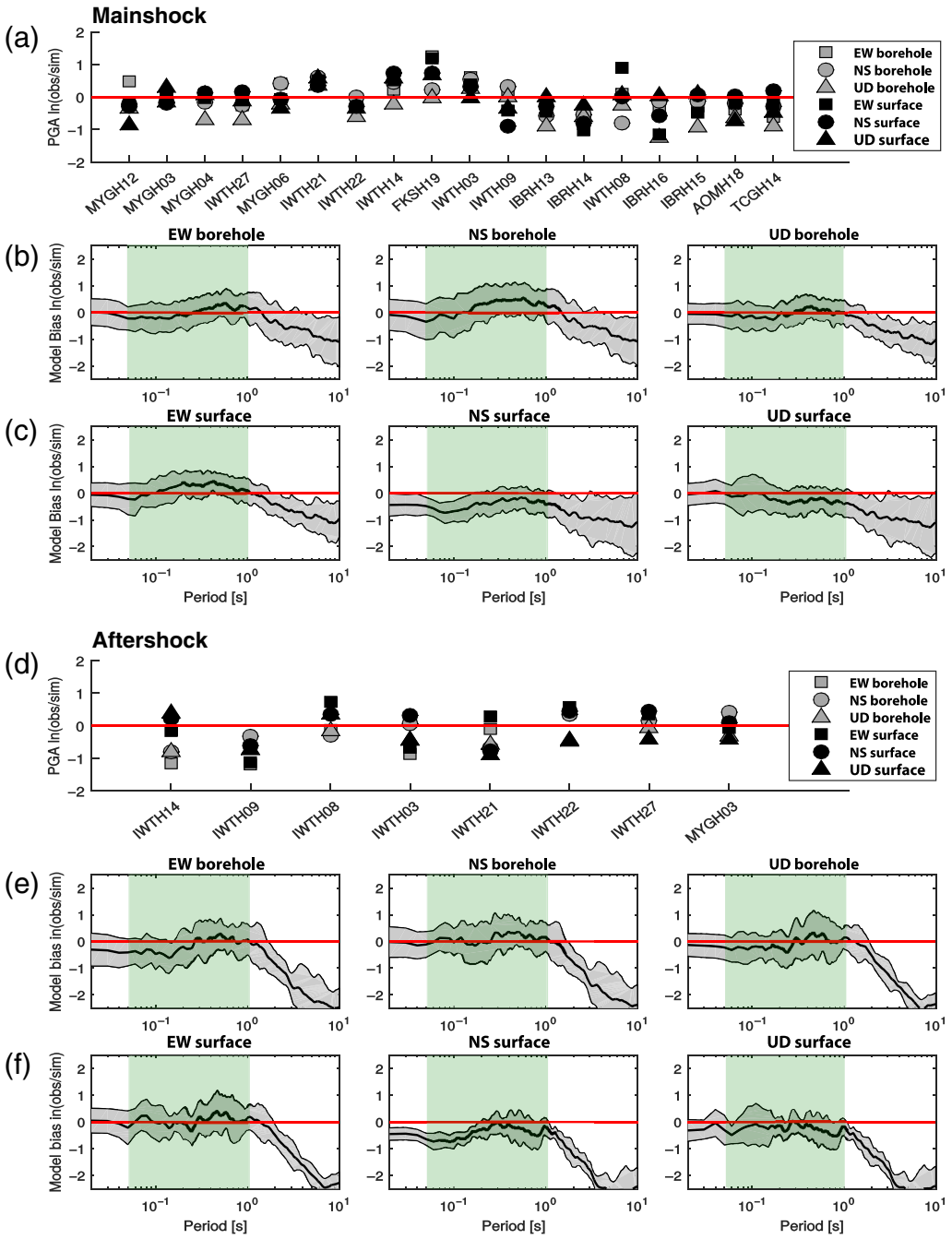

Figure 9. PGA and goodness of fit (GOF) for simulated and observed three-component accelerograms. (a,d) Natural logarithm of the PGA difference between synthetic and observed records for the M_w 9.0 mainshock and the M_w 6.9 aftershock, respectively. (b,e) GOF between observed and simulated acceleration response spectra of 5% damping for borehole station for the M_w 9.0 mainshock and M_w 6.9 aftershock (considering the stress drop of 7 MPa), respectively. (c,f) GOF between observed and simulated acceleration response spectra of 5% damping for a surface station, for the M_w 9.0 mainshock and M_w 6.9 aftershock, respectively. Dashed zones in (b,c,e,f) are periods between a 0.05 and 1 s range, in which our methodology works better. The color version of this figure is available only in the electronic edition.

records on soil sites. We generated synthetic strong-motion records for the M_w 9.0 Tohoku-Oki megathrust earthquake and for the M_w 6.9 aftershock of 23 June 2011. In general, synthetic and real data are in good agreement in time and frequency domains for surface and borehole strong motion in the horizontal and vertical directions for the period band between 0.05 and 1 s.

Data and Resources

KiK-net strong-motion records and *S*-wave velocity profiles were obtained from the National Research Institute for Earth Science and Disaster Resilience (NIED), Japan, webpage (http://www.kyoshin.bosai.go.jp/, last accessed November 2017).

Acknowledgments

This work was supported by the Comisión Nacional de Investigación Científica y Tecnológica CONICYT/FONDECYT Project Number 1170430, PRS (Programa de Riesgo Sísmico) of the University of Chile, and CP thanks to Advanced Mining Technology Center (AMTC FB0809 PIA CONICYT). The authors thank Eduardo Kausel, who generously guided us and shared his codes with us. They thank two anonymous reviewers and the associated editor for their constructive comments and suggestions that improved this work. They thank the support of Graduate Department of Vice-Presidency of Academic Affairs (University of Chile). This study benefited from fruitful discussions with Fabian Bonilla.

References

Aki, K., and P. Richards (2002). *Quantitative Seismology*, Second Ed., University Science Books, Sausalito, California.

Anderson, J., and S. Hough (1984). A model for the shape of the Fourier amplitude spectrum of acceleration at high frequencies, *Bull. Seismol. Soc. Am.* **74,** no. 5, 1969–1993.

Asano, K., and T. Iwata (2012). Source model for strong ground motion generation in the frequency range 0.05–10 Hz during the 2011 Tohoku earthquake, *Earth Planets Space* **64,** no. 12, 6.

Atkinson, G. M., and W. Silva (2000). Stochastic modeling of California ground motions, *Bull. Seismol. Soc. Am.* **90,** no. 2, 255–274.

Beresnev, I. A., and G. M. Atkinson (1997). Modelling finite fault radiation from ω^n spectrum, *Bull. Seismol. Soc. Am.* **87,** 67–84.

Beresnev, I. A., and G. M. Atkinson (1998). FINSIM—A FORTRAN program for simulating stochastic acceleration time histories from finite faults, *Seismol. Res. Lett.* **69,** no. 1, 27–32.

Bonilla, L. F., K. Tsuda, N. Pulido, J. Régnier, and A. Laurendeau (2011). Nonlinear site response evidence of K-NET and KiK-net records from the 2011 off the Pacific coast of Tohoku earthquake, *Earth Planets Space* **63,** no. 7, 50.

Boore, D. M. (1983). Stochastic simulation of high-frequency ground motions based on seismological models of the radiated spectra, *Bull. Seismol. Soc. Am.* **73,** 1865–1894.

Boore, D. M. (2003). Simulation of ground motion using the stochastic method, *Pure Appl. Geophys.* **160,** 635–675.

Boore, D. M. (2009). Comparing stochastic point-source and finite-source ground-motion simulations: SMSIM and EXSIM, *Bull. Seismol. Soc. Am.* **99,** no. 6, 3202–3216.

Boore, D. M., and J. Boatwright (1984). Average body-wave radiation coefficients, *Bull. Seismol. Soc. Am.* **74,** 1615–1621.

Brune, J. N. (1970). Tectonic stress and the spectra of seismic shear waves from earthquakes, *J. Geophys. Res.* **75,** 4997–5009.

Douglas, J., and H. Aochi (2008). A survey of techniques for predicting earthquake ground motions for engineering purposes, *Surv. Geophys.* **29,** no. 3, 187.

Evans, R. (1984). Effects of the free surface on shear wavetrains, *Geophys. J. Roy. Astron. Soc.* **76,** 165–172.

Ghofrani, H., G. M. Atkinson, and K. Goda (2013). Implications of the 2011 M 9.0 Tohoku Japan earthquake for the treatment of site effects in large earthquakes, *Bull. Earthq. Eng.* **11,** no. 1, 171–203.

Ghofrani, H., G. M. Atkinson, K. Goda, and K. Assatourians (2013). Stochastic finite-fault simulations of the 2011 Tohoku, Japan, earthquake, *Bull. Seismol. Soc. Am.* **103,** 1307–1320.

Graves, R. W., and A. Pitarka (2010). Broadband ground-motion simulation using a hybrid approach, *Bull. Seismol. Soc. Am.* **100,** 2095–2123.

Hanks, T. C. (1982). f_{max}, *Bull. Seismol. Soc. Am.* **72,** no. 6A, 1867–1879.

Hanks, T. C., and R. K. McGuire (1981). The character of high-frequency strong ground motion, *Bull. Seismol. Soc. Am.* **71,** 2071–2095.

Hanks, T. C., and M. Wyss (1972). The use of body-wave spectra in the determination of seismic-source parameters, *Bull. Seismol. Soc. Am.* **62,** no. 2, 561–589.

Jiang, J., G. Baird, and D. Blair (1998). Polarization and amplitude attributes of reflected plane and spherical waves, *Geophys. J. Int.* **132,** 577–583.

Joshi, A. (2014). Modeling of strong motion generation areas of the 2011 Tohoku, Japan earthquake using modified semi-empirical technique, *Nat. Hazards* **71,** no. 1, 587–609.

Kamae, K., K. Irikura, and A. Pitarka (1998). A technique for simulating strong ground motion using hybrid Green's function, *Bull. Seismol. Soc. Am.* **88,** no. 2, 357–367.

Kausel, E. (1994). Thin-layer method: Formulation in the time domain, *Int. J. Numer. Methods Eng.* **37,** no. 6, 927–941.

Kausel, E. (2006). *Fundamental Solutions in Elastodynamics: A Compendium*, Cambridge University Press, Cambridge, Massachusetts.

Kausel, E., and J. M. Roësset (1981). Stiffness matrices for layered soils, *Bull. Seismol. Soc. Am.* **71,** no. 6, 1743–1761.

Kurahashi, S., and K. Irikura (2011). Source model for generating strong ground motions during the 2011 off the Pacific coast of Tohoku earthquake, *Earth Planets Space* **63,** no. 7, 11.

Kurahashi, S., and K. Irikura (2013). Short-period source model of the 2011 M_w 9.0 Off the Pacific Coast of Tohoku earthquake, *Bull. Seismol. Soc. Am.* **103,** no. 2B, 1373–1393.

Lay, T. (2017). A review of the rupture characteristics of the 2011 Tohoku-oki M_w 9.1 earthquake, *Tectonophysics* **733,** 4–36, doi: 10.1016/j.tecto.2017.09.022.

Matsubara, M., K. Obara, and K. Kasahara (2008). Three-dimensional *P*- and *S*-wave velocity structures beneath the Japan Islands obtained by high-density seismic stations by seismic tomography, *Tectonophysics* **454,** no. 1, 86–103.

Motazedian, D., and G. M. Atkinson (2005). Stochastic finite-fault modeling based on a dynamic corner frequency, *Bull. Seismol. Soc. Am.* **95,** 995–1010.

Onishi, Y., and M. Horike (2004). The extended stochastic simulation method for close-fault earthquake motion prediction and comments for its application to the hybrid method, *J. Struct. Constr. Eng.* **586,** 37–44.

Otarola, C., and S. Ruiz (2016). Stochastic generation of accelerograms for subduction earthquakes, *Bull. Seismol. Soc. Am.* **106,** no. 6, 2511–2520, doi: 10.1785/0120150262.

Pavlenko, O. V. (2016). Atypical soil behavior during the 2011 Tohoku earthquake ($M_w = 9$), *J. Seismol.* **20,** no. 3, 803–826.

Pulido, N., and T. Kubo (2004). Near-fault strong motion complexity of the 2000 Tottori earthquake (Japan) from a broadband source asperity model, *Tectonophysics* **390,** nos. 1/4, 177–192.

Roten, D., D. Fäh, and L. F. Bonilla (2013). High-frequency ground motion amplification during the 2011 Tohoku earthquake explained by soil dilatancy, *Geophys. J. Int.* **193,** no. 2, 898–904.

Saragoni, G. R., and G. C. Hart (1974). Simulation of artificial earthquakes, *Earthq. Eng. Struct. Dynam.* **2,** 249–267.

Seno, T. (2014). Stress drop as a criterion to differentiate subduction zones where M_w 9 earthquakes can occur, *Tectonophysics* **621,** 198–201.

Tajima, F., J. Mori, and B. L. Kennett (2013). A review of the 2011 Tohoku-Oki earthquake (M_w 9.0). Large-scale rupture across heterogeneous plate coupling, *Tectonophysics* **586,** 15–34.

Udias, A. (1999). *Principles of Seismology*, Cambridge University Press, Cambridge, Massachusetts.

Yagi, Y., and Y. Fukahata (2011). Rupture process of the 2011 Tohoku-Oki earthquake and absolute elastic strain release, *Geophys. Res. Lett.* **38,** L19307, doi: 10.1029/2011GL048701.

Geophysics Department
Universidad de Chile
Blanco Encalada 2002
Santiago, Chile
sruiz@dgf.uchile.cl
(S.R., J.O., C.O.)

Department of Civil Engineering
Universidad de Chile
Blanco Encalada 2002
Santiago, Chile
(C.P., R.S.)

Manuscript received 14 November 2017;
Published Online 4 September 2018